RSC Advances

PAPER

View Article Online
View Journal | View Issue

Cite this: *RSC Adv.*, 2025, **15**, 33758

Inventive pectic acid grafted with polyacrylamide for a highly sensitive and selective non-enzymatic dopamine sensor in pharmaceutical samples

M. S. Hashem *[a] and Hend S. Magar *[b]

Unrivaled polyacrylamide grafted pectic acid (PAAm-*g*-PA) was efficiently produced utilizing a grafting polymerization-derived free radical process. Key reaction conditions were optimized, including initiator concentration, temperature, reaction duration, and monomer concentration. The product's conversion, grafting percentage, and solid content were also estimated. The unique PAAm-*g*-PA was analyzed using Fourier-transform infrared spectroscopy (FT-IR), scanning electron microscopy (SEM) combined with energy dispersive X-ray spectroscopy (EDX), and electrochemical analysis. This inventive PAAm-*g*-PA was used to modify a screen-printed carbon electrode (SPCE) for direct dopamine (DA) electrochemical monitoring *via* cyclic voltammetry (CV) and differential pulse voltammetry (DPV). From the CV analysis, PAAm-*g*-PA/SPCE enhanced electro-catalytic activity towards DA oxidation. According to DPV findings, the developed sensor revealed a linear response for concentrations ranging from 0.01 to 220 μM and a detection limit around 3.0 nM. The PAAm-*g*-PA/SPCE demonstrated good selectivity, stability, and reproducibility. Additionally, the produced sensor showed satisfactory recoveries for pharmaceutical samples.

Received 8th August 2025
Accepted 7th September 2025

DOI: 10.1039/d5ra05810d

rsc.li/rsc-advances

1. Introduction

A class of polysaccharides known as pectins includes pectin, protopectin, pectinic acid, and pectic acid.[1,2] Unlike pectin, pectic acid (PA) is a hydrophobic biopolymer present in some vegetables and overripe fruits. It is created during fruit ripening when pectin is broken down by pectinase. Early fruit development results in water-insoluble protopectin, which protopectinase then transforms into pectin.[3] Fruits that are too ripe transform into pectic acid, which is insoluble in water, making them unsuitable for making hydrogel materials. Distributing PA in aqueous media using hydrophilic polymer material is necessary to force it to create a cross-linked hydration network. Polyacrylamide (PAAm), a linear hydrophilic synthetic macromolecule, is applied as a binder and stabilizer, thickener, and suspender in cosmetics, paper, waste treatment, and stabilization of soil fields, respectively.[4,5] Green and non-toxic polyacrylamide does not have a vinyl group, although it is produced from the polymerization of acrylamide, which is a possible neurotoxin at elevated levels.[6] Thus, PAAm is extensively utilized in biomedical applications encompassing wound healing,[7] tissue engineering,[8] drug administration systems,[9] and the separation of biomolecules.[10] It is also used as an electrochemical sensing electrode because the material possesses proteolytic reaction-based redox-sensitive resonating structures.[11] It is utilized in the formulation of the electroactive and conductive polymeric network matrices that are applied in sensor fields such as the detection of riboflavin,[12] lead(II) ions,[13] hydrogen peroxide,[14] glucose,[15] hemoglobin,[16] and dopamine.[17]

Dopamine (DA), first identified in 1957, is a brain chemical neurotransmitter that influences the cardiovascular, central nervous system, circulatory, endocrine glands, and kidney systems.[18,19] It also regulates body functions like attentiveness, recall, learning, locomotion, emotional state, conduct, and mental cognition.[20,21] Imbalances in DA concentrations within the human brain can induce addiction, depressive symptoms, schizophrenia, and neurological diseases.[22] Thus, an accurate, direct, straightforward, selectable, and sensitive approach is required for DA monitoring concentrations within the human body system. Various techniques have been explored to determine DA levels, including chemiluminescence, chromatography, colorimetry, fluorescence, and spectrometry.[23–25] These traditional procedures necessitate time-consuming and costly sample preparation.[26,27] Electrochemical detection technique[28] has gained significant interest mainly because of its affordability,[29] simplicity,[30] rapid response time,[31] low detection limit,[32] exceptional sensitivity,[33] and specificity.[34,35] Polymeric materials such as pectic acid, gelatin,[36] cellulose,[37] and polyacrylates[38,39] serve in the modification of screen-printed electrodes for electrochemical sensing fields.

[a]*Polymers and Pigments Department, National Research Centre, Dokki, P. O. Box 12622, Giza, Egypt. E-mail: ms.hashem@nrc.sci.eg*

[b]*Applied Organic Chemistry Department, National Research Centre, Dokki, P. O. Box 12622, Giza, Egypt. E-mail: hendamer2000@yahoo.com*

The main goal of this work is to synthesize an innovative PAAm-*g*-PA as a highly sensitive and selective dopamine electrochemical sensor for pharmaceutical samples. As far as we know, only our published research has explored pectic acid in sensor applications. The original development of PAAm-*g*-PA was achieved through a grafting polymerization procedure triggered by free radicals. Optimal conditions for the grafting polymerization process involving initiator concentrations, reaction duration, temperature, and monomer concentrations were studied. PAAm-*g*-PA's conversion, grafting percentage, and solid content were also determined. The creatively grafted pectic acid was analyzed through spectroscopic and electrochemical methods. The electrochemical performance of the PAAm-*g*-PA/SPCE towards the DA detection was analyzed using voltammetric techniques. PAAm-*g*-PA improved the electrocatalytic activity for DA detection compared to the unmodified PA and other research in the literature. Another crucial feature of the DA sensor is its ease of setup, low detection limit (LOD), and broad linear concentration ranges. The manufactured sensor efficacy was explored in pharmaceutical samples containing DA through the DPV approach in conjunction with the standard addition procedure, achieving satisfactory recovery percentages.

2. Experimental methods

2.1. Materials and apparatus

Pectic acid (PA) was acquired from Fluka. Acrylamide (AAm) and ammonium persulfate (APS) were purchased from Merck. Dopamine (DA) was obtained from Solarbio Life Science. Uric acid (UA), ascorbic acid (AA), potassium chloride (KCl), potassium ferricyanide ($K_3[Fe(CN)_6]$), and potassium ferrocyanide ($K_4[Fe(CN)_6]\cdot 3H_2O$) were bought from Pio CHEM. MPBio was the source of the phosphate buffer saline (PBS) tablets, having a pH of 7.4. Zensors Company provided the 50 × 13 mm ($h \times w$) screen-printed carbon electrodes (SPCE). All the remaining solvents and compounds were of laboratory quality and did not require additional purification. Each test was conducted using double-distilled water (DDW).

The morphological surface of the polymeric materials was examined by scanning electron microscope (SEM), accompanied by an energy dispersive X-ray spectrometer (EDX). Fourier-transformed infrared (FT-IR) spectra data were recorded with a PerkinElmer Spectrum 400 FT-IR spectrometer. Electrochemical studies were achieved by cyclic voltammetry (CV), differential pulse voltammetry (DPV), and electrochemical impedance spectroscopy (EIS) through a CHI 660 electrochemical workstation at ambient temperature (25 ± 2 °C). These investigations were carried out using a screen-printed carbon electrode system (SPCE) that included three electrodes: a carbon working modified electrode called PAAm-*g*-PA/SPCE with a diameter of 3.0 mm of graphitic carbon, a counter electrode made of carbon, and a reference electrode made of silver.

2.2. Methods

2.2.1. Synthesis of polyacrylamide-*g*-pectic acid. PAAm-*g*-PA was accomplished through grafting polymerization mediated by a free radical procedure. Ultrasonic vibrations were used to mix 1 g of PA with a 2% AAm solution until complete dispersion produced an off-white colloid. Once the colloid was generated, it was added to the polymerization reservoir with 0.15 g of APS dissolved in 10 mL of DDW. A perfectly uniform colloidal solution was created after the polymerization reaction was moderately stirred utilizing a magnetic bar for 2 hours at 70 °C. The developed mixture was then spread onto a Petri dish, dried for 24 hours in an oven at 40 °C, and stored for further research.

2.2.2. Percentage calculations of conversion, grafting, and solid content. The created PAAm-*g*-PA's conversion, grafting percentage, and solid content were calculated using eqn (1), (2), and (3), respectively.[40,41]

$$\text{Conversion } (\%) = \frac{\text{weight of grafted PA} - \text{weight of PA}}{\text{weight of AAm}} \times 100 \quad (1)$$

$$\text{SC } (\%) = \frac{\text{weight of PAAm-}g\text{-PA after drying}}{\text{weight of PAAm-}g\text{-PA before drying}} \times 100 \quad (2)$$

$$G\ (\%) = \frac{\text{weight of grafted PA} - \text{weight of PA}}{\text{weight of PA}} \times 100 \quad (3)$$

2.2.3. The electrode modulations method. A commercial SPCE featured a carbon working electrode, a carbon counter electrode, and an integrated silver/silver chloride reference electrode. A 5 mg mL^{-1} solution of PA or PAAm-*g*-PA was prepared in DDW, and then a fixed volume of 5 μL was dropped-cast onto the surface of the working electrode. The modulated electrodes were then air-dried at room temperature to ensure stable and uniform film formation.

2.2.4. Electrochemical characterization studies. The CV and EIS assessments were replicated three times, utilizing 5.0 mM of ($K_3[Fe(CN)_6]$) as the typical redox probe and 0.1 M of KCl as the supporting electrolyte. Every EIS assessment was performed within a frequency range of 100 000 to 0.1 Hz, at open circuit potential, with an amplitude of 10 mV. CV measurements were taken by cycling the voltage from −0.4 V to +0.7 V at a scan rate of 50 mV s^{-1}. Fitting the gathered Nyquist plots with analogous Randles circuits allowed identification of all EIS influencing variables involved capacitive phase elements (CPEs), charge transfer resistance (R_{ct}), resistance of solution (R_s), and Warburg resistance diffusion (W).

2.2.5. Dopamine detection with the modulated working electrodes. A 5.0 mg mL^{-1} aqueous homogeneous dispersion of PAAm-*g*-PA was equipped and ultrasonicated for 1 hour. A fine layer of the grafted biopolymer was deposited by drop-casting 10 μL from its suspension on the SPCE's working surface. After that, the produced PAAm-*g*-PA/SPCE was dehydrated for the entire night at an ambient temperature. DPV and CV were employed to identify the detection limit and analyze the dopamine redox reaction. In the CV measurements, the potential was cycled between −0.4 V and +0.7 V at a scan rate of 50 mV s^{-1}, while in the DPV experiments, the potential ranged from 0.0 V

to −0.4 V. For comparison, the same procedure was followed to prepare PA/SPCE electrodes.

2.2.6. Detecting dopamine in pharmaceutical samples. To assess DA levels in dosage-form pharmaceutical samples obtained from Ibn Hayyan Pharmaceutical Industries and SUNNY MEDICAL without requiring extra pre-treatment, a freshly created PAAm-*g*-PA/SPCE sensor has been used. The electrochemical cell held 3.0 mL of PBS and was supplemented with 10 μL of the pharmaceutical substances. DA concentrations were measured using an adapted DPV assay with potential values ranging between 0.0 V and −0.4 V with a scan rate of 50 mV s^{-1}.

3. Results and discussions

3.1. Synthesis and characterization of PAAm-*g*-PA

Hydrophobic PA was subjected to ultrasonication with AAm solution to form a naked eye homogeneous colloidal solution as a result of an amide linkage formation between the –COOH group of PA and the $–NH_2$ group of AAm,[42] as explained throughout Scheme 1. The pectic acid skeleton was then grafted with polyacrylamide (PAAm-*g*-PA) through an easily performed free radical polymerization procedure with APS as an initiator, as illustrated in Scheme 1. PA radicals were generated when the sulfate radicals from APS were formed at 70 °C, leading to the removal of hydrogen atoms from the hydroxyl groups of PA.[43–45] Thanks to the structure of PA, it could fulfill three functions: acting as a polysaccharide skeleton, a macromolecular radical for acrylamide polymerization, and a green cross-linker for interpenetrating acrylate polymeric network formulations.[46,47] A study was conducted on factors influencing the grafting polymerization process, including APS concentration, AA concentration, reaction duration, and temperature, as outlined in Table 1. Regarding the free radical-driven grafting polymerization procedure, 1 g of AAm, 0.15 g of APS, a reaction temperature of 65 °C, and a reaction period of 2 hours were the ideal variables. This optimized PAAm-*g*-PA formulation was used in subsequent analysis and studies. Additionally, the grafted polymer's solid content, conversion, and grafting percentage were determined and shortened in Table 1. When the colloid polymeric combination was applied to a watch glass, its viscosity increased with higher PA and AAm concentrations. The inclusion of PA during molding produced a semi-transparent

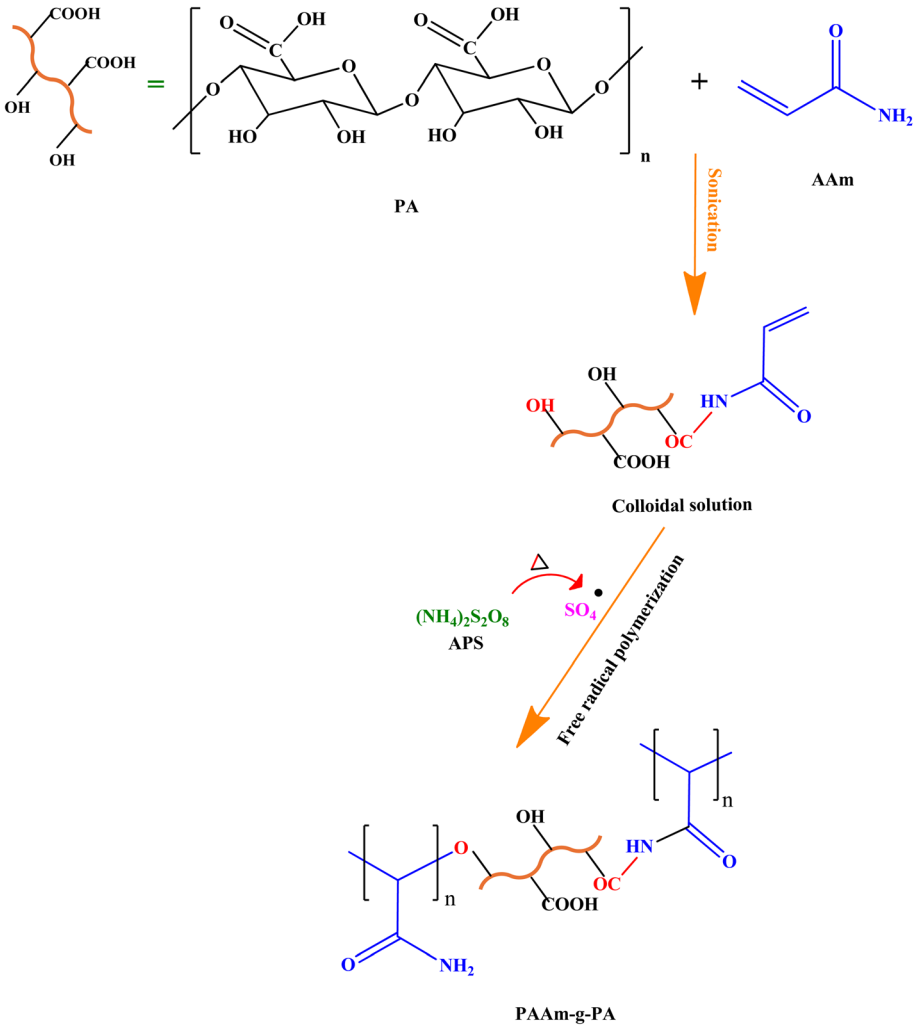

Scheme 1 Schematic representation for the suggested grafting polymerization mechanism of PA with PAAm triggered by a free radical.

Table 1 Parameters and optimal conditions for PAAm-*g*-PA preparation

	SC (%)	Conversion (%)	*G* (%)
Temperature (°C)			
60	1.2	56.7	114.1
70	3.7	98.9	267.4
80	3.1	98.6	263.2
Reaction duration (min)			
60	0.9	52.3	117.1
120	3.8	99.5	266.5
180	3.3	98.7	265.2
APS concentration (g)			
0.075	1.6	51.6	115.3
0.15	3.9	98.2	266.8
0.3	3.6	96.1	253.4
AAm concentration (g)			
1	1.1	57.5	120.2
2	3.9	99.1	265.9
3	3.2	97.2	259.7

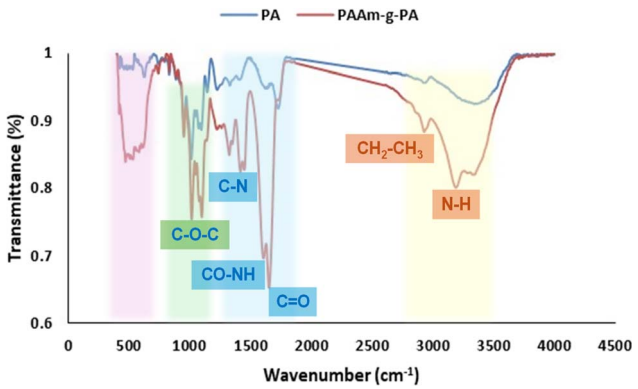

Fig. 1 The FT-IR spectral analysis of PA and PAAm-*g*-PA.

film with an off-white color. The produced PAAm-*g*-PA was analyzed utilizing FT-IR, SEM, EDX, and electrochemical approaches.

3.2. FT-IR spectra

The PAAm-*g*-PA and PA structures and their characteristic peaks were analyzed based on FT-IR spectroscopy at wavenumbers spanning from 400 to 4000 cm^{-1}, corresponding to Fig. 1. Within the PA spectral range, the stretching vibration of the OH group was responsible for the broad band around 3340 cm^{-1}, whereas the stretching vibration of the C=O group was related to the band at about 1728 cm^{-1}. Bands around 1225 cm^{-1}, 1094 cm^{-1}, and 1012 cm^{-1} were linked to the vibrational stretching of the C–O–C bond, whereas the band close to 1401 cm^{-1} showed the stretching vibration of the C–OH. Within the PAAm-*g*-PA spectral range, a new characteristic stretching vibration band of N–H of PAAm emerged at 3188 cm^{-1}, merging into the wide range of 3100 to 3400 cm^{-1}. Additional bands nearest to 2927 cm^{-1} and 1325 cm^{-1} were observed due to the CH_2–CH_3 bending and C–H stretching vibration of AAm, respectively. Bands near 1606 cm^{-1} and 1449 cm^{-1}, which correspond to CO–NH and asymmetric stretching vibration C–N, respectively, verified the establishment of the amide linkage that existed among PAA and PAAm. The FT-IR results confirmed the successful creation of PAAm-*g*-PA.

3.3. Morphological and elemental composition studies

Morphological appearance and elemental composition for PA and PAAm-*g*-PA were explored through a scanning electron microscope (SEM) and an energy-dispersive X-ray spectroscopy (EDX). Fig. 2a illustrates that PA exhibited hollow layers resembling wavy leaves longitudinally and transversely, with multiple spaces between them. EDX outcomes revealed the existence of C and O. The spaces between the layers of PA were filled with PAAm, resulting in regular, one-way, non-hollow layers with smooth surfaces and delicate undulations, as seen in Fig. 2b. The EDX results for PAAm-*g*-PA showed the inclusion of C, O, and N, confirming grafting of the PA skeleton with PAAm.

3.4. CV and EIS explorations of PAAm-*g*-PA

The electrochemical attitudes for modified screen-printed carbon electrodes (SPCEs) were evaluated *via* CV and EIS in an electrolyte mixture containing 0.1 M of KCl and 5.0 mM of $[Fe(CN)_6]^{3-/4-}$ acting as the oxidation–reduction probe. CV evaluations were performed with a scan rate of 50 mV s^{-1} throughout potential values ranging between −0.4 V and +1.0 V. As shown in Fig. 3a and Table 2, the PAAm-*g*-PA/SPCE had a much greater faradaic current response (325 μA) than the PA/SPCE (176 μA) and the bare (unmodified) SPCE (120 μA). The $[Fe(CN)_6]^{3-/4-}$ oxidation–reduction pair was responsible for this improved redox response, suggesting better electron transport kinetics on the PAAm-*g*-PA-modified surface. Further insight into the interfacial charge transfer resistance was obtained *via* EIS, which was indicated in Fig. 3b.[48] R_{ct} at the interface between the electrode and electrolyte was represented *via* a clear semicircle in the low-frequency area across Nyquist plots, which were recorded spanning the frequency from 100 kHz to 100 mHz. Experimental results were plugged into an equivalent electrical circuit model to determine the R_{ct} values for each electrode configuration. The R_{ct} value decreased significantly for the PAAm-*g*-PA/SPCE ($R_{ct} = 19\ \Omega$) compared to the PA/SPCE ($R_{ct} = 500\ \Omega$) and the bare SPCE ($R_{ct} = 950\ \Omega$), according to Table 2. This decrease is explained by PAAm-*g*-PA's increased electrical conductivity, likely due to the complementary action of amino and carboxylic functional groups, facilitating effective electron transfer. Based on these findings, the PAAm-*g*-PA/SPCE was chosen for additional use in electrochemical sensing because of its superior surface conductivity and electron transport properties.

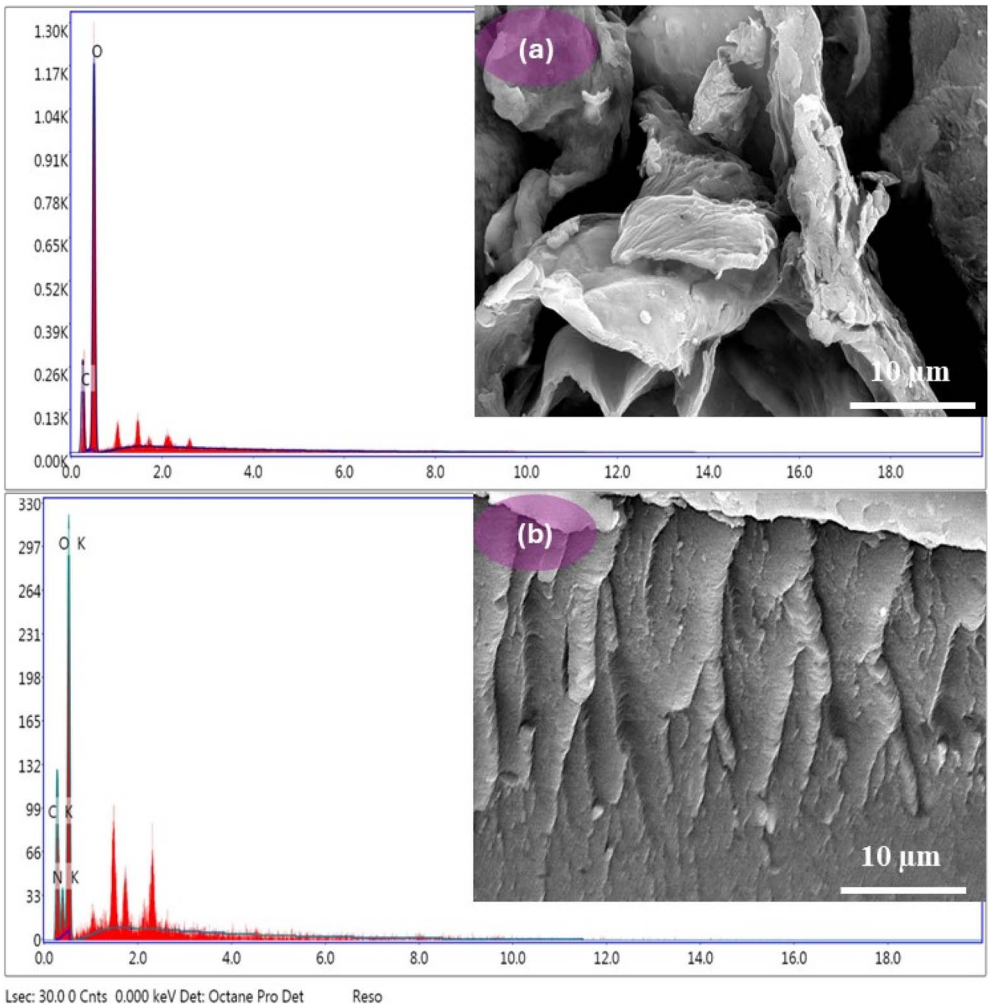

Fig. 2 SEM and EDX pictures of (a) PA and (b) PAAm-*g*-PA.

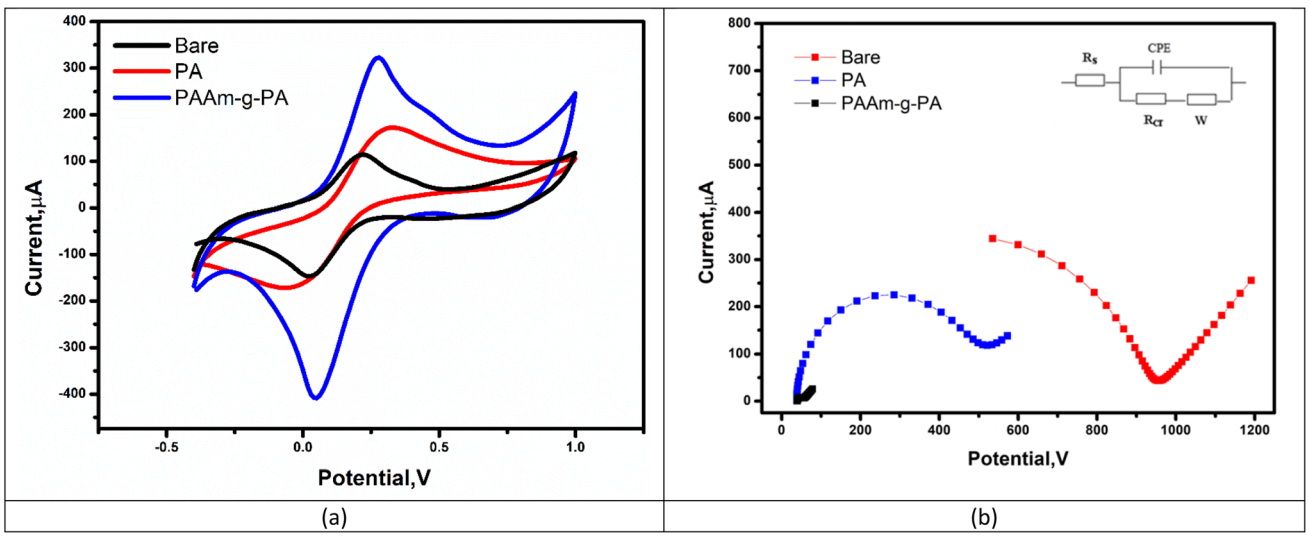

Fig. 3 (a) CV and (b) EIS (the figure inset depicts the circuit that was utilized to fit the EIS data). For bare (unmodulated), PA, beside PAAm-*g*-PA/SPCE in a solution containing 5 mM $[Fe(CN)_6]^{3-/4-}$, with a scan rate of 50 mV s^{-1} for cyclic voltammetry measurements.

Table 2 Summary of electrochemical parameters extracted from Fig. 3a and b[a]

Electrode type	I_{pa} (μA)	I_{pc} (μA)	$E_{oxd.}$ (V)	$E_{red.}$ (V)	R_s (Ω)	R_{ct} (Ω)	CPE (μF)	n	W (Ω)
Bare (unmodified)	120	−151	0.22	0.033	32	950	13.5	0.89	162
PA	176	−170.9	0.33	−0.045	36	500	34.1	0.91	105
PAAm-*g*-PA	325	−412	0.28	0.04	37	19	102.4	0.85	43

[a] I_{pa}, I_{pc}, $E_{oxd.}$, $E_{red.}$ denote the current anodic peak, the current cathodic peak, the oxidation potential, and the reduction potential, respectively. CPE, R_{ct}, R_s, and W represent the capacitive phase element, the resistance of charge transfer, the resistance of the solution, and the diffusion of Warburg resistance, respectively.

3.5. Optimization of experimental conditions

Voltammetric tests were conducted at various scan rates throughout the ferro/ferri cyanide (FCN) solution to understand the electrochemical characteristics[49] of PAAm-*g*-PA/SPCEs. The experiments involved plotting the square root of the scan rate against the current using the FCN redox system to evaluate the fundamental electrochemical behavior and surface properties for the modulated SPCEs. FCN is a well-characterized, reversible redox probe that provides consistent and reproducible signals, making it ideal for assessing electron transfer kinetics, surface area, and diffusion characteristics at the electrode interface.[50] As the applied scan rates rose, the redox current also rose linearly across each electrode employed, as seen through Fig. 4(a–f). However, PAAm-*g*-PA set up the maximum output in linear redox processes when the scan rate was further increased, as observed in Fig. 4e. Based on the equation of Randles–Ševčík:

$$I_p = 2.69 \times 10^5 \times n^{3/2} \times A \times D^{1/2} \times C \times \nu^{1/2}$$

where the I_p, n, D, A, C, and ν reflect the current oxidation peak (amperes), the transferred electron numbers, the diffusion coefficient ($cm^2\ s^{-1}$), the surface area of electrochemically active materials (cm^2), FCN concentration (molarity), and the rate of scan ($V\ s^{-1}$), respectively.

A plot of the FCN redox reactions' current anodic peak (I_{pa}) and current cathodic peak (I_{pc}) against the square roots of the scan rates, according to Fig. 4f. An excellent linear relationship with a correlation coefficient of about 0.9966 was observed, allowing the active surface area determination for the unmodulated electrode compared to the modulated electrode with PA and PAAm-*g*-PA. All the modulated electrodes showed a considerable increase in active surface area; the unmodulated SPCE measured 0.054 cm^2, while PA/SPCE and PAAm-*g*-PA/SPCE were 0.217 and 0.3072 cm^2, respectively. Remarkably, the SPCE modulated with PAAm-*g*-PA exhibited almost a five-fold rise in the active surface area of the electrodes.

The pronounced enhancement of the FCN redox signal observed at PAAm-*g*-PA/SPCE, compared to the bare SPCE, can be attributed to several contributing factors. Firstly, R_{ct} played a critical role contrary to the common expectation that non-conductive polymeric films impede electron transfer, EIS data, as stated by Fig. 3b, demonstrated PAAm-*g*-PA/SPCE exhibition of a lower R_{ct} than the unmodulated electrode. This indicated that the grafted polymeric matrix preserved and actively enhanced charge transfer kinetics at the electrode interface. Secondly, the hydrated and porous structure of PAAm-*g*-PA contributed significantly. The hydrogel-like polymer layer swelled upon exposure to aqueous environments, creating a highly porous and hydrated interface. This facilitates improved ion mobility and diffusion of redox-active species, effectively increasing the electroactive surface area available to FCN. Thirdly, specific interactions between functional groups and FCN were likely influential. The abundant –COOH and CO–NH functionalities within the PA and PAAm chains might be engaged in electrostatic interactions or hydrogen bonding with FCN ions. These interactions could lead to localized enrichment or favorable orientation of FCN near the electrode surface, enhancing the redox response. Lastly, the improved wettability and surface affinity of PAAm-*g*-PA/SPCE further supported its enhanced performance. The hydrophilic nature of the polymeric film promoted superior contact between the electrode surface and the aqueous electrolyte, ensuring more efficient access of redox probes for the active sites.

3.6. Dopamine redox reaction at modulated electrode surface

CV results, as shown throughout Fig. 5a, revealed that PAAm-*g*-PA/SPCE exhibited a markedly higher anodic peak current for dopamine oxidation than the unmodulated SPCE. This enhancement suggests an increased effective electroactive surface area and improved adsorption of dopamine molecules at the electrode interface; both contributed to enhancing sensitivity. From the CV curves recorded at varying scan rates ranging from 0.05 to 0.7 $V\ s^{-1}$ for the dopamine redox reaction, conforming to Fig. 5b, the modulated electrodes demonstrated a significant increase in current with increasing scan rate. A plot of I_{pa} *versus* the square root of the scan rate, in line with Fig. 5c, revealed an excellent linear relationship for the electrodes modified with PA and PAAm-*g*-PA, with a correlation coefficient (R^2) of approximately 0.9966. This strong linearity indicates a diffusion-controlled electrochemical process, which was further confirmed by a log I_p *versus* log scan rate plot showing a slope close to 0.5, depending on Fig. 5d. Such a slope is characteristic of diffusion-controlled behavior, where the peak current is proportional to the square root of the scan rate, as described by the Randles–Ševčík equation. This implies that the redox process is governed primarily by the diffusion of dopamine from the bulk solution to the electrode surface, rather than surface adsorption phenomena or kinetic limitations. These findings confirm that the modified electrode with PAAm-*g*-PA facilitated efficient diffusion-driven electron transfer

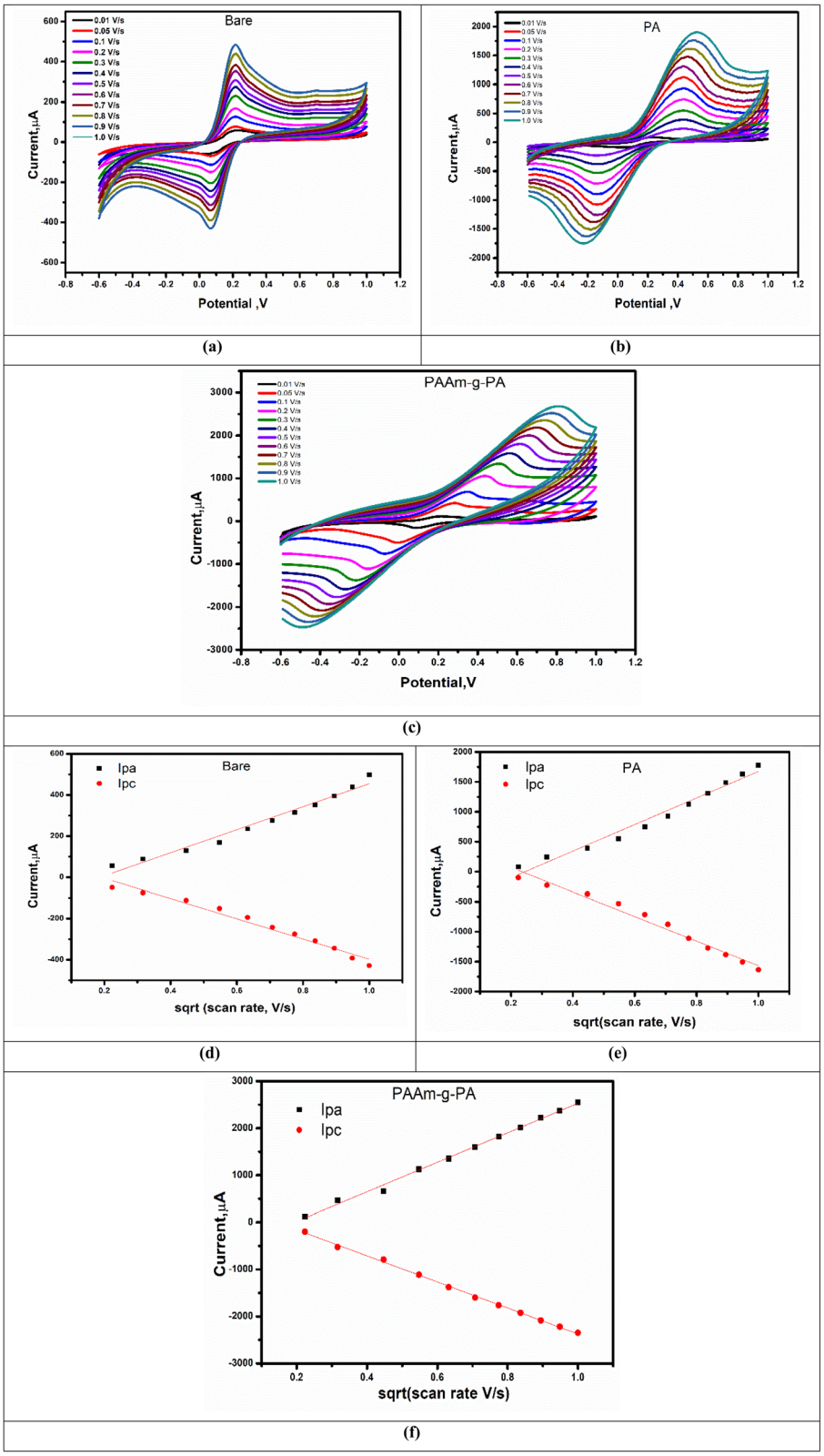

Fig. 4 CV data illustrated the effect of scan rate on the FCN redox reactions at modified SPCEs. Continuous rise in the currents of oxidation–reduction peak as the scan rate rose for (a) the unmodified (bare), (b) PA, and (c) PAAm-*g*-PA. The relationship between the current and the scan rates square roots of (d) unmodified (bare), (e) PA, and (f) PAAm-*g*-PA.

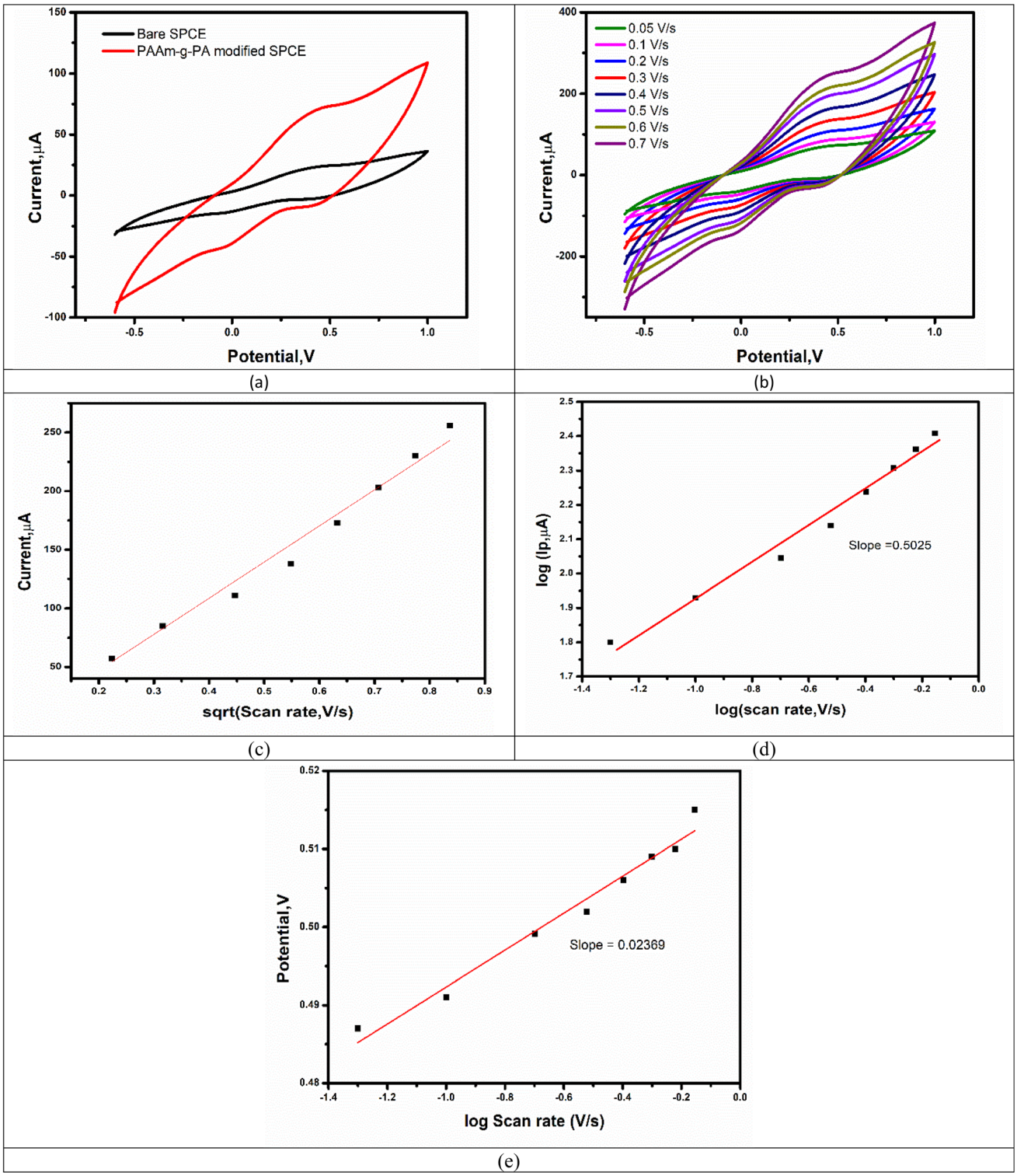

Fig. 5 (a) CV curves of bare (unmodified) and PAAm-*g*-PA/SPCEs. (b) The effect of varying scan rates (0.05–0.7 V s^{-1}) on the redox behavior of dopamine (100 μM at PAAm-*g*-PA/SPCE). (c) Linear relationship between I_{pa} and the square root of the scan rate, indicating diffusion-controlled kinetics. (d) log–log plot of I_p *versus* scan rate, with a slope close to 0.5, further confirming a diffusion-controlled electrochemical process. (e) Peak potential value *versus* the square root of scan rates.

during the dopamine oxidation–reduction process. A systematic shift in the anodic peak potential with increasing scan rate was observed in the cyclic voltammetry measurements, as shown in Fig. 5e. This behavior is indicative of a quasi-reversible electron transfer process. Moreover, the anodic peak current exhibited a linear relationship with the square root of the scan rate,

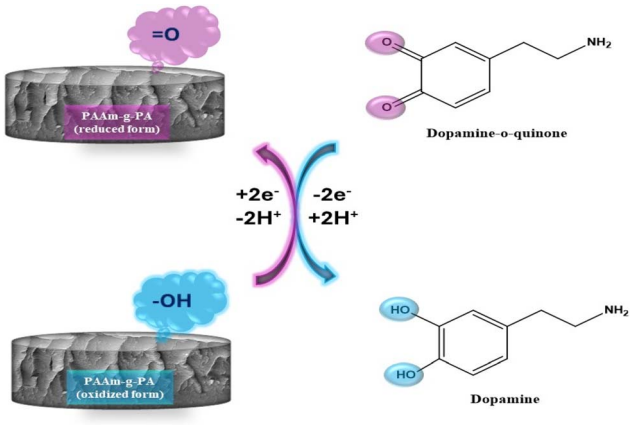

Scheme 2 DA redox reaction mechanism.

suggesting a diffusion-controlled mechanism. The relationship between the oxidative peak potential (E_p) and the logarithm of the scan rate ($\log \nu$) followed the linear regression equation:

$$E_p\ (\mathrm{V}) = 0.02368 \log \nu + 0.516\ (R^2 = 0.987)$$

This correlation is consistent with Laviron's equation for irreversible or quasi-reversible systems:

$$E_p = E_0^{'} + \left(\frac{RT}{\alpha n F}\right)\log\left(\frac{RTk_0}{\alpha n F}\right) + \left(\frac{RT}{\alpha n F}\right)\log \nu$$

where $E_0^{'}$ is the formal potential (V), R is the universal gas constant (8.314 J mol^{-1} K^{-1}), T is the absolute temperature (298.15 K), α is the electron transfer coefficient (assumed to be 0.5), n is the number of electrons involved in the redox process, and F is the Faraday constant (96 485 C mol^{-1}).

From the slope of E_p against $\log \nu$ plot and assuming $\alpha = 0.5$, the number of electrons (n) involved in the oxidation of dopamine was calculated to be two. This supported the proposed voltammetric oxidation mechanism of dopamine, involving a two-electron transfer process, as illustrated in Scheme 2. The underlying mechanism for enhanced dopamine detection can be attributed to selective pre-concentration *via* electrostatic and hydrogen bonding interactions at the electrode interface. At physiological pH, dopamine exists predominantly in its protonated, positively charged form. In contrast, the pectic acid component of PAAm-*g*-PA/SPCE contains deprotonated carboxyl groups, while the polyacrylamide chains present amide functionalities capable of hydrogen bonding. These negatively charged and polar functional groups act as specific interaction sites for dopamine molecules. Electrostatic attraction between the cationic dopamine and the anionic carboxyl groups, along with hydrogen bonding between dopamine's hydroxyl groups and the amide moieties, promoted effective accumulation of dopamine at the electrode surface. This localized enrichment increases the effective concentration of dopamine in the vicinity of the electrode, thereby amplifying the oxidation current and improving the overall sensitivity of the detection system.

3.6.1. DPV measurements. DPV showed a high sensitivity in detecting small electroactive compounds like dopamine for precise quantitative analysis; therefore, DPV will be allocated and adjusted in the following sections. PAAm-*g*-PA/SPCE demonstrated exceptional electrochemical and electrocatalytic activity. DPV variables such as selectivity, accumulation duration, and the impact of the supporting electrolyte's pH were tested to optimize analytical results. The pH value of the supporting electrolyte significantly influenced the electrochemical responses for the suggested electrodes. Therefore, PBS containing 180 μM of DA and pH values between 5.0 and 9.0 was

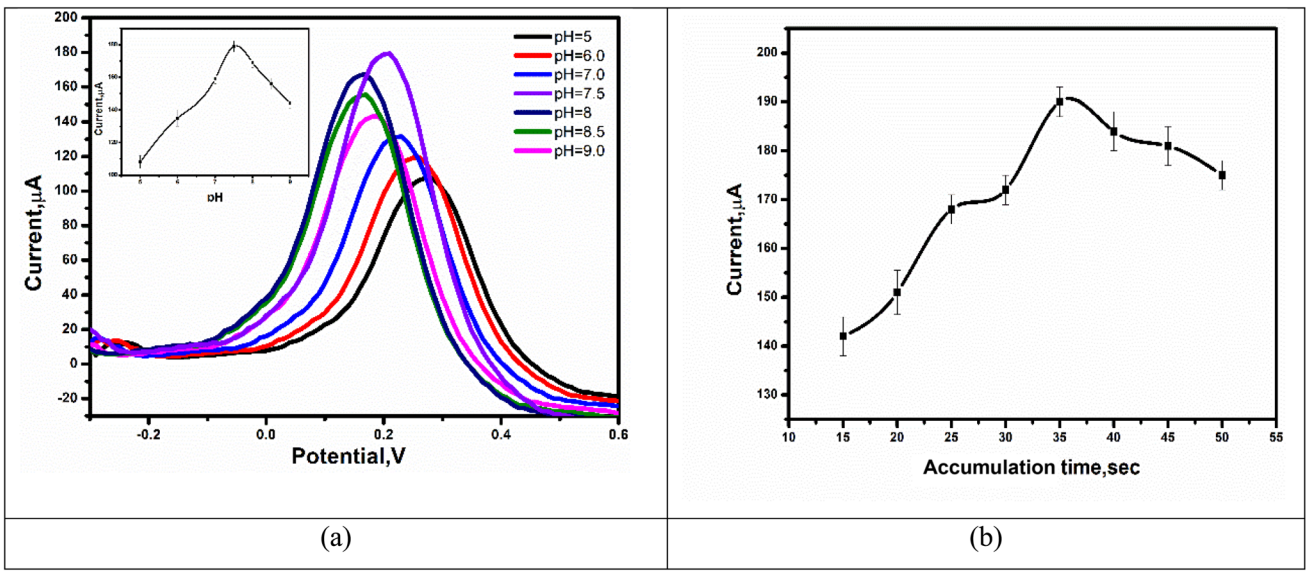

Fig. 6 (a) DPV and pH values bar diagram against the peak of electrical current (inset figure) for 180 μM of DA in PBS at pH 7.5 with a deposition time of 35 seconds, beside a scan rate of 50 mV s^{-1}. (b) Time of accumulation against the electrical current response in PBS at pH 7.5 with 180 μM of DA at a scan rate of 50 mV s^{-1}.

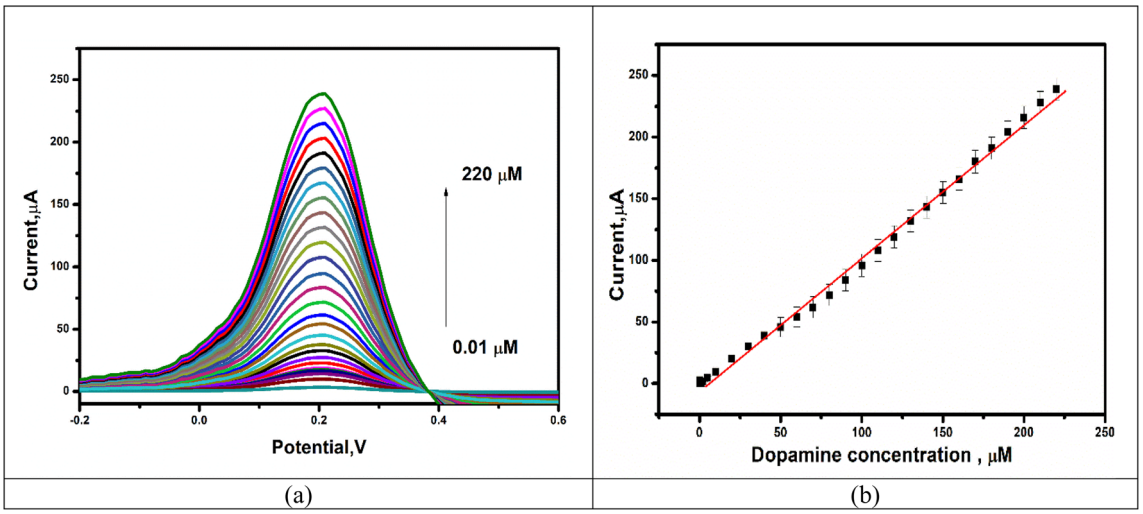

Fig. 7 (a) DPV curves for various DA levels (0.01–220 μM) in PBS at pH 7.5 using PAAm-*g*-PA/SPCE. (b) Calibration curves of various DA concentrations *via* peak current.

used to investigate the electrocatalytic efficiency of PAAm-*g*-PA/SPCE, as represented in Fig. 6a. The electrical current oxidation peak of DPV rose from 5 to 7.5 before falling, leading to the selection of PBS at pH 7.5 for all dopamine DPV electrochemical analyses. Electroactive species numbers presented at the surface of the electrode dictated the peak current magnitude. Thus, the DPV technique was used using PAAm-*g*-PA/SPCE in PBS at pH 7.5 with 180 μM of DA, to investigate the time of accumulation impact on the DA electrical current anodic peak near a scan rate of 50 mV s^{-1}. The current oxidation peak value rose over 15 to 35 seconds before falling, as illustrated in Fig. 6b. The decline in peak electrical current 30 seconds later could be attributed to how saturated the electrode surface was with DA. As a result, the optimal accumulation time for further experimental studies was determined to be 30 seconds. Fig. 7a displayed an outstanding calibration curve linearity at a dynamic broad range of DA levels between 0.01 and 220 μM. As observed in Fig. 7b, significant linearity was achieved with an overall correlation coefficient R^2 of around 0.991 and a low standard deviation across all dopamine additions. Based on the DPV calibration curve, the detection limit and limit quantification values were 3 nM and 6 nM, respectively. This method demonstrated an extremely high sensitivity (1.0729 μA μM^{-1}) with a low LOD, making it among the most accurate and sensitive electrochemical approaches for DA detection reported.

3.6.2. Reproducibility and stability of PAAm-*g*-PA/SPCE. Seven identical sensors were created and tested for dopamine detection under the same circumstances to evaluate the reproducibility of the PAAm-*g*-PA/SPCEs, as indicated by Fig. 8a. The ensuing dopamine oxidation peak currents demonstrated excellent fabrication consistency and reproducible sensor performance, with a relative standard deviation (RSD) around 2.94%. PAAm-*g*-PA/SPCEs showed limited reusability due to surface fouling from dopamine oxidation products and

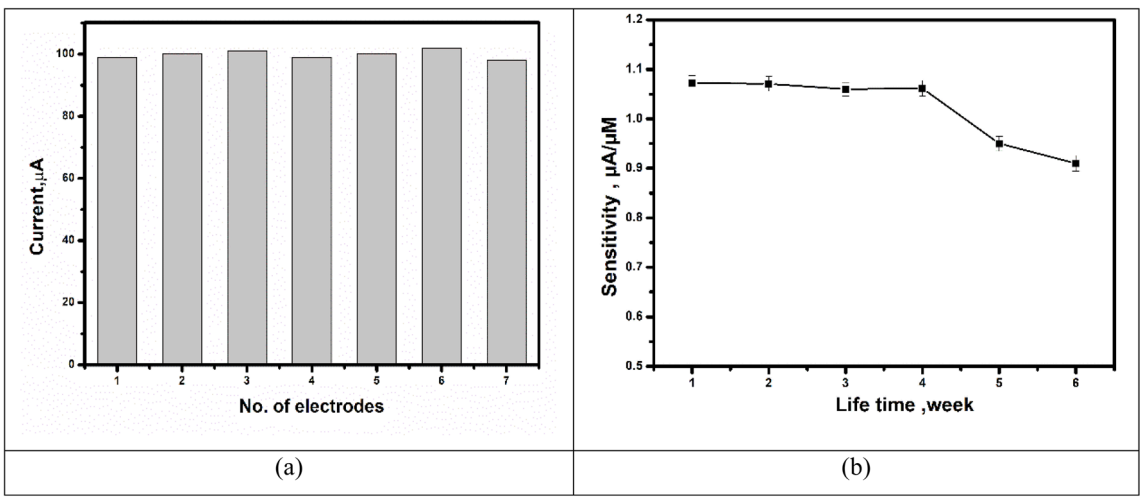

Fig. 8 (a) Reproducibility and (b) lifetime of PAAm-*g*-PA/SPCE toward DA detection in PBS with pH 7.5.

Table 3 Comparison of DPV methods for DA detection using various modified electrode materials[a]

Electrode materials	Electrolyte	Method	Linear range (μM)	Detection limit (μM)	Ref.
Au–Cu_2O/rGO	PBS	DPV	10–90	3.9	51
N-rGO	PBS (pH 7)	DPV	3–70	1.5	52
Au/PDDA/GNs	PBS (pH 7)	DPV	2–28	1.0	53
PdAu/rGO	PBS (pH 7)	DPV	1.25–73.75	0.75	54
AG–NA	PBS (pH 7.4)	DPV	0.5–35	0.33	55
GNP/FTO	PBS (pH 7)	DPV	30–100	0.22	56
PGE	PBS (pH 6.8)	DPV	0.2–8	0.20	57
NGF	PBS (pH 7.4)	DPV	0.1–80	0.030	58
PANI–rGO–NF/GCE	PBS (pH 5)	DPV	0.05–60	0.024	59
β-CD/rGO	PBS (pH 7.5)	DPV	0.05–50	0.017	60
PA/GO/GCE	PBS (pH 7)	DPV	0.05–10	0.016	61
Pt–Ag/Gr	PBS (pH 6.5)	DPV	0.1–60	0.012	62
Graphene/GCE	PBS (pH 7)	DPV	4–100	2.64	63
SWCNT/Fe_2O_3/GCE	PBS (pH 7)	SWV	3.2–31.8	0.36	64
Pt/rGO/MnO_2/GCE	PBS (pH 7)	DPV	1.5–215	0.1	65
WO_3/GCE	PBS (pH 7)	DPV	0.1–50, 50–600	0.024	66
NiHCF/PNH/AuE	PBS (pH 7)	DPV	0.1–4.3, 4.3–9.6	0.021	67
CuO nano-leaf	PBS (pH 8)	DPV	1–7.5, 7.5–140	0.5	68
ZnO nanorod/flower like CuO/AuE	PBS (pH 7.3)	CA	1000–8000	100	69
CuHCC nanocubes/GCE	PBS (pH 7.2)	DPV	0.1–350	0.019	70
Mn/Cu oxides@CNTs-SPCE	PBS (pH 7.4)	DPV	0.001–140	0.0003	71
PAAm-*g*-PA	PBS (pH 7.5)	DPV	0.01–220	0.003	This work

[a] Chronoamperometry method (CA), glassy-carbon electrode (GCE), gold electrode (AuE), and screen-printed carbon electrode (SPCE).

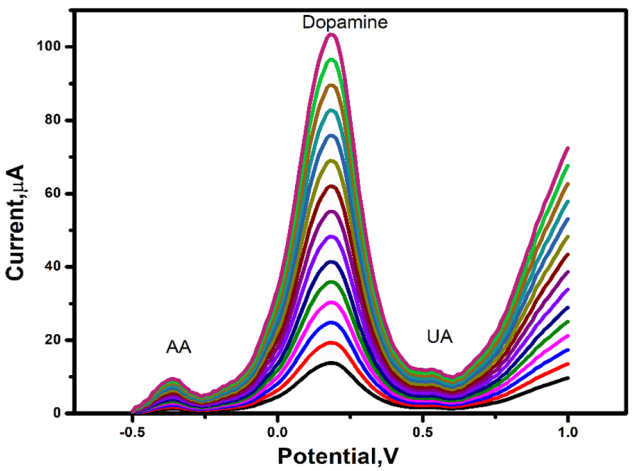

Fig. 9 DPV responses for varied DA concentrations with varying AA and UA concentrations in PBS at pH 7.5, using the PAAm-*g*-PA/SPCE.

Table 4 DPV-based determination of DA in pharmaceutical formulations using PAAm-*g*-PA/SPCE

Sample	Added (μM)	Found (μM) ± SD	Recovery (%)
1	0.1	0.11 ± 0.02	110
2	1	0.9 ± 0.05	90
3	10	9.8 ± 0.2	98
4	20	19.9 ± 0.3	99.5
5	30	29.8 ± 0.4	99.3
6	50	49.3 ± 0.5	98.6

a gradual loss of sensitivity. After one measurement cycle, the current response typically declined, indicating that the modified electrodes are best used as single-use disposable sensors. The operational lifetime and stability of the modulated electrodes were assessed over a month, since the DA oxidation current was weakly detected when the electrodes were refrigerated. However, the electrochemical response showed good long-term performance, remaining stable for up to three weeks and only experiencing a 15% drop in the current of the oxidation peak after a month, as displayed across Fig. 8b. A comparison of the suggested PAAm-*g*-PA/SPCE with other dopamine detectors utilizing various electrode modifications employing DPV was presented in Table 3. The data illustrated that this new PAAm-*g*-PA/SPCE sensor had lower detection limits and greater linear detection ranges than numerous published works, emphasizing its superior analytical capability for dopamine monitoring.

3.6.3. Selectivity of PAAm-*g*-PA modified SPCEs. For dopamine sensors, selectivity is a crucial factor,[72] especially when dealing with coexisting electroactive molecules that could oxidize within the same potential range. DPV was used to analyze possible interfering chemicals, including ascorbic acid (AA) and uric acid (UA), to evaluate the PAAm-*g*-PA/SPCE selectivity. Clear resolution from the DA signal was made possible by the discrete oxidation peaks produced by each interferent at a different voltage, as revealed in Fig. 9. When the sensitivity of PAAm-*g*-PA/SPCEs with DA in the presence of interfering chemicals was compared to that in their absence, the sensitivity decreased by about 4.3%. The slope was 1.053 μA μM^{-1} when interferents were present and 1.072 μA μM^{-1} when they were not. This slight decrease demonstrated the improved

electrode's excellent selectivity for dopamine detection, even in complex sample matrices.

3.6.4. Injection samples analysis. The PAAm-*g*-PA/SPCE was evaluated following the standard addition procedure on commercial 200 mg mL^{-1} of DA hydrochloride injection samples to determine its practical application for pharmaceutical sample analysis. After transferring a measured aliquot from each ampoule straight into the electrochemical cell, DPV was carried out. The samples underwent two consecutive DA administrations following the initial evaluation, resulting in recovery values ranging from 98.0% to 110.0%, indicating sensor accuracy, as summarized in Table 4. These outcomes validate the potential of the developed sensor for precise dopamine measurement in pharmaceutical products. This successful application further demonstrated the adaptability and usefulness of the method in everyday electrochemical analysis; it also acts as proof-of-concept for applying the technique to other products.

4. Conclusions

In summary, an innovative PAAm-*g*-PA was synthesized through a grafting polymerization-derived free radical process regarding direct DA electrochemical monitoring within pharmaceutical samples. The optimal conditions affecting the polymerization reaction involving the concentration of APS and AAm, temperature, and reaction duration were investigated. The resulting polymer's conversion, grafting percentage, and solid content were also measured. PAAm-*g*-PA was characterized by FT-IR, SEM, and EDX, alongside electrochemical techniques. SPCEs served as the platform for performing electrochemical measurements *via* CV and EIS, besides optimizing and analyzing DPV. Modulating SPCEs with the PAAm-*g*-PA significantly enhanced their electrochemical and electrocatalytic performance, enabling efficient and direct dopamine oxidation. The developed DPV method exhibited excellent linearity across a wide concentration range between 0.01 and 220 μM, ultra-high sensitivity, and achieved LOD as low as 3.0 nM. The sensor's excellent selectivity was maintained even when common electroactive interferents such as UA and AA were present. The PAAm-*g*-PA/SPCE sensor was successfully applied to pharmaceutical samples, achieving high recovery rates, thereby confirming the method's practical utility and reliability for DA quantification in complex matrices.

Author contributions

M. S. Hashem: conceptualization, writing – review & editing, visualization, formal analysis, investigation, data curation. Hend S. Magar: conceptualization, writing – review & editing, visualization, formal analysis, investigation, data curation.

Conflicts of interest

The authors state that there are no conflicts of interest.

Data availability

The data supporting this study's findings are available on request from the corresponding author, [M. S. Hashem].

Acknowledgements

This research was funded by the National Research Centre in Giza, Egypt, under internal project ID 13020103.

References

1 P. Sharma, C. Bhandari, S. Kumar, B. Sharma, P. Bhadwal and N. Agnihotri, *Diet, Microbiome and Health Handbook of Food Bioengineering*, 2018, pp. 299–345.
2 M. A. Abd El-Ghaffar and M. S. Hashem, Grafted Pectin with Glycidyl Methacrylate for Multi-Sites Urease Immobilization, *J. Compos. Biodegrad. Polym.*, 2017, **5**(2), 62–73.
3 A. Nighojkar, M. K. Patidar and S. Nighojkar, Pectinases: Production and Applications for Fruit Juice Beverages, *Processing and Sustainability of Beverages, Volume 2: The Science of Beverages*, 2019, ch. 8, pp. 235–273.
4 M. Doble and A. Kumar, Degradation of Polymers, *Biotreatment of Industrial Effluents*, 2005, ch. 9, pp. 101–110.
5 F. A. Andersen, Amended final report on the safety assessment of polyacrylamide and acrylamide residues in cosmetics, *Int. J. Toxicol.*, 2005, **24**, 21–50.
6 P. K. Bairagi and N. Verma, Electro-polymerized polyacrylamide nano film grown on a Ni-reduced graphene oxide-polymer composite: A highly selective non-enzymatic electrochemical recognition element for glucose, *Sens. Actuators, B*, 2019, **289**, 216–225.
7 D. Bhardwaj, R. Bhaskar, A. K. Sharma, M. Garg, S. S. Han and G. Agrawal, Gelatin/Polyacrylamide-Based Antimicrobial and Self-Healing Hydrogel Film for Wound Healing Application, *ACS Appl. Bio Mater.*, 2024, **7**(2), 879–891, DOI: **10.1021/acsabm.3c00903**.
8 Y. Geng, T. Liu, M. Zhao, H. Wei, X. Yao and Y. Zhang, Silk fibroin/polyacrylamide-based tough 3D printing scaffold with strain sensing ability and chondrogenic activity, *Composites, Part B*, 2024, **271**, 111173.
9 S. S. Sana, S. K. Arla, V. Badineni, *et al.*, Development of poly(acrylamide-co-diallyldimethylammoniumchloride) nanogels and study of their ability as drug delivery devices, *SN Appl. Sci.*, 2019, **1**, 1716, DOI: **10.1007/s42452-019-1742-3**.
10 N. Sharma, R. Sharma, Y. S. Rajput, B. Mann, R. Singh and K. Gandhi, Separation methods for milk proteins on polyacrylamide gel electrophoresis: Critical analysis and options for better resolution, *Int. Dairy J.*, 2021, **114**, 104920.
11 Y. Endo, M. Kawaguchi and T. Kato, Synthesis of poly [(methyl methacrylate)-co-acrylamide] modified by titanium-triisopropoxide and their thermal stability, *Polymer*, 2002, **43**, 3863–3872.
12 M. S. Hashem and H. S. Magar, Creative synthesis of pH-dependent nanoporous pectic acid grafted with acrylamide and acrylic acid copolymer as an ultrasensitive and

selective riboflavin electrochemical sensor in real samples, *Int. J. Biol. Macromol.*, 2024, **280**, 136022.

13 B. Niazy, H. Ghasemzadeh, A. Keshtkar Vanashi and S. Afraz, Polyvinyl alcohol/polyacrylamide hydrogel-based sensor for lead(II) ion sensing by resonance Rayleigh scattering, *React. Funct. Polym.*, 2022, **175**, 105266.

14 A. J. Xie, Q. X. Liu, H. L. Ge and Y. Kong, Novel H_2O_2 electrochemical sensor based on graphene–polyacrylamide composites, *Mater. Technol.*, 2014, **30**(1), 50–53, DOI: 10.1179/1753555714Y.0000000203.

15 Y. Kim, H. Namgung and T. S. Lee, Synthesis of a glucose oxidase-conjugated, polyacrylamide-based, fluorescent hydrogel for a reusable, ratiometric glucose sensor, *Polym. Chem.*, 2016, **7**, 6655–6661.

16 S. Wu, W. Tana and H. Xu, Protein molecularly imprinted polyacrylamide membrane: for haemoglobin sensing, *Analyst*, 2010, **135**, 2523–2527.

17 T. Zhang, X. Xuan, M. Li, C. Li, P. Li and H. Li, Molecularly imprinted Ni-polyacrylamide-based electrochemical sensor for the simultaneous detection of dopamine and adenine, *Anal. Chim. Acta*, 2022, **1202**, 339689.

18 V. K. Yeragani, M. Tancer, P. Chokka and G. B. Baker, Arvid Carlsson, and the story of dopamine, *Indian J. Psychiatry*, 2010, **52**, 87–88.

19 D. Kim, S. Lee and Y. Piao, Electrochemical determination of dopamine and acetaminophen using activated graphene-Nafion modified glassy carbon electrode, *J. Electroanal. Chem.*, 2017, **794**, 221–228.

20 H. W. Yu, J. H. Jiang, Z. Zhang, G. C. Wan, Z. Y. Liu, D. Chang and H. Z. Pan, Preparation of quantum dots CdTe decorated graphene composite for sensitive detection of uric acid and dopamine, *Anal. Biochem.*, 2017, **519**, 92–99.

21 J. Fang, Z. Xie, G. Wallace and X. Wang, Co-deposition of carbon dots and reduced graphene oxide nanosheets on carbon-fiber microelectrode surface for selective detection of dopamine, *Appl. Surf. Sci.*, 2017, **412**, 131–137.

22 V. Sharma, A. Sundaramurthya, A. Tiwari and A. K. Sundramoorthy, Graphene nanoplatelets-silver nanorods-polymer based in situ hybrid electrode for electroanalysis of dopamine and ascorbic acid in biological samples, *Appl. Surf. Sci.*, 2018, **449**, 558–566.

23 L. Q. Xie, Y. H. Zhang, F. Gao, Q. A. Wu, P. Y. Xu, S. S. Wang, N. N. Gao and Q. X. Wang, A highly sensitive dopamine sensor based on a polyaniline/reduced graphene oxide/Nafion nanocomposite, *Chin. Chem. Lett.*, 2017, **28**, 41–48.

24 P. Wiench, Z. González, R. Menéndez, B. Grzyb and G. Gryglewicz, Beneficial impact of oxygen on the electrochemical performance of dopamine sensors based on N-doped reduced graphene oxides, *Sens. Actuators, B*, 2018, **257**, 143–153.

25 A. Ejaz, Y. Joo and S. Jeon, Fabrication of 1,4-bis(aminomethyl) benzene and cobalt hydroxide@graphene oxide for selective detection of dopamine in the presence of ascorbic acid and serotonin, *Sens. Actuators, B*, 2017, **240**, 297–307.

26 Y. Haldorai, A. T. E. Vilian, M. Rethinasabapathy, Y. S. Huh and Y. K. Han, Electrochemical determination of dopamine using a glassy carbon electrode modified with TiN-reduced graphene oxide nanocomposite, *Sens. Actuators, B*, 2017, **247**, 61–69.

27 X. Liu, E. Shangguan, J. Li, S. Ning, L. Guo and Q. Li, A novel electrochemical sensor based on FeS anchored reduced graphene oxide nanosheets for simultaneous determination of dopamine and acetaminophen, *Mater. Sci. Eng., C*, 2017, **70**, 628–636.

28 H. S. Magar and A. M. Fahim, Sensing platform based on RGO/cellulose-triazole composite for the electrochemical detection of mercury(II) ions in food samples, *Microchem. J.*, 2025, **215**, 114243.

29 H. A. S. Tohamy and H. S. Magar, A Flexible, Low-Cost, Disposable Non-Enzymatic Electrochemical Sensor Based on MnO_2/Cellulose Nanostructure, *ECS J. Solid State Sci. Technol.*, 2022, **11**(12), 127003.

30 H. S. Magar, R. Y. A. Hassan and M. N. Abbas, Non-enzymatic disposable electrochemical sensors based on CuO/Co_3O_4@MWCNTs nanocomposite modified screen-printed electrode for the direct determination of urea, *Sci. Rep.*, 2023, **13**(1), 2034.

31 H. S. Magar, P. K. Brahman and R. Y. A. Hassan, Disposable impedimetric nano-immunochips for the early and rapid diagnosis of Vitamin-D deficiency, *Biosens. Bioelectron.: X*, 2022, **10**, 100124.

32 A. M. Mansour, H. S. Magar, A. Elzwawy, A. B. Abou Hammad and A. M. El Nahrawy, Structural, optical, and electrochemical properties of tungsten-doped cadmium zinc phosphate nanoporous materials for energy storage and peroxide detection, *RSC Adv.*, 2025, **15**, 15670–15693.

33 H. S. Magar, H. Abdelghany, M. N. Abbas, U. Bilitewski and R. Y. A. Hassan, Fast analysis of Staphylococcus aureus in food products using disposable label-free nano-electrochemical immunosensor chips, *Microchem. J.*, 2023, **193**, 109097.

34 H. S. Magar, M. Fayez, F. Febbraio and R. Y. A. Hassan, Esterase-2 mutant-based nanostructured amperometric biosensors for the selective determination of paraoxon (Neurotoxin), *Anal. Biochem.*, 2025, **698**, 115751.

35 H. S. Magar, B. A. Hemdan, H. R. M. Rashdan and R. Y. A. Hassan, Rapid and Selective Detection of Foodborne Pathogens Using a Disposable Bio-sensing System Designed by Stepwise Antibody Immobilization on AuNPs@Cu-MOF Nanocomposite, *J. Anal. Test.*, 2024, **8**, 478–492.

36 H. S. Magar, A. M. Fahim and M. S. Hashem, Accurate, affordable, and easy electrochemical detection of ascorbic acid in fresh fruit juices and pharmaceutical samples using an electroactive gelatin sulfonamide, *RSC Adv.*, 2024, **14**, 39820–39832.

37 H. S. Magar, E. E. A. E. Magd, R. Y. A. Hassan and A. M. Fahim, Rapid impedimetric detection of cadmium ions using Nanocellulose/ligand/nanocomposite (CNT/Co_3O_4), *Microchem. J.*, 2022, **182**, 107885.

38 M. S. Hashem, H. S. Magar, A. M. Fahim and R. A. Sobh, Antioxidant-rich brilliant polymeric nanocomposites for

quick and efficient non-enzymatic hydrogen peroxide sensor, *RSC Adv.*, 2024, **14**(19), 13142–13156.

39 H. S. Magar, M. S. Hashem and R. A. Sobh, Design of metal oxide nanoparticles-embedded polymeric nanocomposites for hydrogen peroxide chronoamperometric sensor, *Polym. Compos.*, 2024, **45**(4), 3653–3665.

40 M. S. Hashem, R. A. Sobh and M. A. Abd El-Ghaffar, pH-responsive bionanocomposite pectin grafted with dimethylaminoethyl methacrylate and acrylic acid copolymer along with silver nanoparticles for breast cancer drug delivery, *Polym. Eng. Sci.*, 2024, **64**(12), 6115–6128, DOI: 10.1002/pen.26975.

41 M. S. Hashem, R. A. Sobh, A. M. Fahim and G. H. Elsayed, Alginate sulfonamide hydrogel beads for 5-fluorouracil delivery: antitumor activity, cytotoxicity assessment, and theoretical investigation, *Int. J. Biol. Macromol.*, 2024, **282**(Part 1), 136573.

42 G. Cravotto and Z. Wu, The use of power ultrasound for green organic synthesis: Sonochemical organic reactions in aqueous media, in *Power Ultrasonics*, ed. J. A. Gallego-Juárez, K. F. Graff and M. Lucas, Woodhead Publishing Series in Electronic and Optical Materials, Woodhead Publishing, 2nd edn, 2023, ch. 37, pp. 833–859.

43 M. A. Abd El-Ghaffar, M. S. Hashem, M. K. El-Awady and A. M. Rabie, pH-sensitive sodium alginate hydrogels for riboflavin controlled release, *Carbohydr. Polym.*, 2012, **89**(2), 667–675.

44 M. S. Hashem, H. S. Magar, A. M. Fahim and R. A. Sobh, Antimicrobial, antioxidant, mechanistic, docking simulation, and electrochemical studies for grafting polymerization of novel sulphonated gelatin derived from chicken feet, *Mater. Chem. Phys.*, 2023, **310**, 128474.

45 M. A. Abd El-Ghaffar and M. S. Hashem, Calcium alginate beads encapsulated PMMA-g-CS nano-particles for α-chymotrypsin immobilization, *Carbohydr. Polym.*, 2013, **92**, 2095–2102.

46 S. Regina, T. Poerio, R. Mazzei, C. Sabia, R. Iseppi and L. Giorno, Pectin as a non-toxic crosslinker for durable and water-resistant biopolymer-based membranes with improved mechanical and functional properties, *Eur. Polym. J.*, 2022, **172**, 111193.

47 L. Khedmat, A. Izadi, V. Mofid and S. Y. Mojtahedi, Recent advances in extracting pectin by single and combined ultrasound techniques: A review of techno-functional and bioactive health-promoting aspects, *Carbohydr. Polym.*, 2020, **229**, 115474.

48 X. Pang, W. Liu, Z. Zheng, X. Zheng, J. Wang, Q. Wang, L. Niu and F. Gao, Hybridization-driven synchronous regeneration of biosensing interfaces for Listeria monocytogenes based on recognition of fullerol to single- and double-stranded DNA, *Food Chem.*, 2024, **461**, 140906.

49 R. A. Sobh, H. S. Magar, A. M. Fahim and M. S. Hashem, Construction, molecular docking simulation and evaluation of electrochemical properties of polymeric nanospheres comprising novel synthesized monomer via green microemulsion polymerization, *Polym. Adv. Technol.*, 2024, **35**(1), e6248.

50 R. A. Sobh and H. S. Magar, Innovative formulation of a functional nano-copolymer derived from glycidyl methacrylate and acrylonitrile as an exceptionally sensitive and selective electrochemical sensor for folic acid detection in pharmaceutical and food samples, *Nanoscale*, 2025, **17**, 18359–18376.

51 T. K. Aparna, R. Sivasubramanian and M. A. Dar, One-pot synthesis of Au-Cu_2O/rGO nanocomposite based electrochemical sensor for selective and simultaneous detection of dopamine and uric acid, *J. Alloys Compd.*, 2018, **741**, 1130–1141.

52 P. Wiench, Z. González, R. Menéndez, B. Grzyb and G. Gryglewicz, Beneficial impact of oxygen on the electrochemical performance of dopamine sensors based on N-doped reduced graphene oxides, *Sens. Actuators, B*, 2018, **257**, 143–153.

53 H. Wang, L. G. Xiao, X. F. Chu, Y. D. Chi and X. T. Yang, Rational design of gold nanoparticle/graphene hybrids for simultaneous electrochemical determination of ascorbic acid, dopamine and uric acid, *Chin. J. Anal. Chem.*, 2016, **44**(12), 1617–1625.

54 C. Zou, J. Zhong, S. Li, H. Wang, J. Wang, B. Yan and Y. Du, Fabrication of reduced graphene oxide-bimetallic PdAu nanocomposites for the electrochemical determination of ascorbic acid, dopamine, uric acid and rutin, *J. Electroanal. Chem.*, 2017, **805**, 110–119.

55 D. Kim, S. Lee and Y. Piao, Electrochemical determination of dopamine and acetaminophen using activated graphene-Nafion modified glassy carbon electrode, *J. Electroanal. Chem.*, 2017, **794**, 221–228.

56 M. M. Rahman, N. S. Lopa, M. J. Ju and J. J. Lee, Highly sensitive and simultaneous detection of dopamine and uric acid at graphene nanoplatelet-modified fluorine-doped tin oxide electrode in the presence of ascorbic acid, *J. Electroanal. Chem.*, 2017, **792**, 54–60.

57 Y. Wang, Y. Huang, B. Wang, T. Fang, J. Chen and C. Liang, Three-dimensional porous graphene for simultaneous detection of dopamine and uric acid in the presence of ascorbic acid, *J. Electroanal. Chem.*, 2016, **782**, 76–83.

58 X. Ding, J. Bai, T. Xu, C. Li, H. M. Zhang and L. Qu, A novel nitrogen-doped graphene fiber microelectrode with ultrahigh sensitivity for the detection of dopamine, *Electrochem. Commun.*, 2016, **72**, 122–125.

59 L. Q. Xie, Y. H. Zhang, F. Gao, Q. A. Wu, P. Y. Xu, S. S. Wang, N. N. Gao and Q. X. Wang, A highly sensitive dopamine sensor based on a polyaniline/reduced graphene oxide/Nafion nanocomposite, *Chin. Chem. Lett.*, 2017, **28**, 41–48.

60 M. Cheng, X. Zhang, M. Wang, H. Huang and J. Ma, A facile electrochemical sensor based on well-dispersed graphene-molybdenum disulfide modified electrode for highly sensitive detection of dopamine, *J. Electroanal. Chem.*, 2017, **786**, 1–7.

61 D. Wang, F. Xu, J. Hu and M. Lin, Phytic acid/graphene oxide nanocomposites modified electrode for electrochemical sensing of dopamine, *Mater. Sci. Eng., C*, 2017, **71**, 1086–1089.

62 N. S. Anuar, W. J. Basirun, Md. Shalauddin and S. Akhter, A dopamine electrochemical sensor based on a platinum–silver graphene nanocomposite modified electrode, *RSC Adv.*, 2020, **10**, 17336.
63 Y. R. Kim, *et al.*, Electrochemical detection of dopamine in the presence of ascorbic acid using graphene modified electrodes, *Biosens. Bioelectron.*, 2010, **25**, 2366–2369, DOI: **10.1016/j.bios.2010.02.031**.
64 A. S. Adekunle, B. O. Agboola, J. Pillay and K. I. Ozoemena, Electrocatalytic detection of dopamine at single-walled carbon nanotubes–iron(III) oxide nanoparticles platform, *Sens. Actuators, B*, 2010, **148**, 93–102.
65 B. Yang, *et al.*, A three dimensional Pt nanodendrite/graphene/MnO_2 nanoflower modified electrode for the sensitive and selective detection of dopamine, *J. Mater. Chem. B*, 2015, **3**, 7440–7448.
66 A. C. Anithaa, N. Lavanya, K. Asokan and C. Sekar, WO_3 nanoparticles based direct electrochemical dopamine sensor in the presence of ascorbic acid, *Electrochim. Acta*, 2015, **167**, 294–302.
67 M. H. Mashhadizadeh, T. Yousefi and A. Nozad Golikand, A nickel hexacyanoferrate and poly(1-naphthol) hybrid film modified electrode used in the selective electroanalysis of dopamine, *Electrochim. Acta*, 2012, **59**, 321–328.
68 Z. Zheng, *et al.*, Selective electrochemical determination of dopamine in serum in the presence of ascorbic acid and uric acid by using a CuO nanoleaf electrode, *Anal. Methods*, 2014, **6**, 7923–7927.
69 K. Khun, *et al.*, An electrochemical dopamine sensor based on the ZnO/CuO nanohybrid structures, *J. Nanosci. Nanotechnol.*, 2014, **14**, 6646–6652.
70 N. Karikalan, M. Velmurugan, S. M. Chen and K. Chelladurai, A copper hexacyanocobaltate nanocubes based dopamine sensor in the presence of ascorbic acid, *RSC Adv.*, 2016, **6**, 48523–48529.
71 H. S. Magar, E. S. M. Duraia and R. Y. A. Hassan, Dopamine fast determination in pharmaceutical products using disposable printed electrodes modified with bimetal oxides carbon nanotubes nanocomposite, *Sci. Rep.*, 2025, **15**, 11229.
72 Z. Zhang, L. Huang, F. Gao, Z. Zheng, Y. Lin, S. Wang, Q. Wang and Q. Wang, A ratiometric electrochemical sensor for antiepileptic drug of carbamazepine based on electroactive Ni^{2+}-terephthalic acid MOF, *Talanta*, 2025, **292**, 128019.